2014

Active control of magnetoresistance of organic spin valves using ferroelectricity

Dali Sun
Fudan University

Mei Fang
Fudan University

Xiaoshan Xu
University of Nebraska-Lincoln, xiaoshan.xu@unl.edu

Lu Jiang
Oak Ridge National Laboratory

Hangwen Guo
Oak Ridge National Laboratory

See next page for additional authors

Authors

Dali Sun, Mei Fang, Xiaoshan Xu, Lu Jiang, Hangwen Guo, Yanmei Wang, Wenting Yang, Lifeng Yin, Paul C. Snijders, T. Z. Ward, Zheng Gai, X. -G. Zhang, Ho Nyung Lee, and Jian Shen

ARTICLE

Active control of magnetoresistance of organic spin valves using ferroelectricity

Dali Sun[1,2,3,*,†], Mei Fang[1,*], Xiaoshan Xu[2], Lu Jiang[2,3], Hangwen Guo[2,3], Yanmei Wang[1], Wenting Yang[1], Lifeng Yin[1], Paul C. Snijders[2,3], T.Z. Ward[2], Zheng Gai[2,4], X.-G. Zhang[4,5], Ho Nyung Lee[2] & Jian Shen[1,3]

Organic spintronic devices have been appealing because of the long spin lifetime of the charge carriers in the organic materials and their low cost, flexibility and chemical diversity. In previous studies, the control of resistance of organic spin valves is generally achieved by the alignment of the magnetization directions of the two ferromagnetic electrodes, generating magnetoresistance. Here we employ a new knob to tune the resistance of organic spin valves by adding a thin ferroelectric interfacial layer between the ferromagnetic electrode and the organic spacer: the magnetoresistance of the spin valve depends strongly on the history of the bias voltage, which is correlated with the polarization of the ferroelectric layer; the magnetoresistance even changes sign when the electric polarization of the ferroelectric layer is reversed. These findings enable active control of resistance using both electric and magnetic fields, opening up possibility for multi-state organic spin valves.

[1] State Key Laboratory of Surface Physics and Department of Physics and Collaborative Innovation Center of Advanced Microstructure, Fudan University, Shanghai 200433, China. [2] Materials Science and Technology Division, Oak Ridge National Laboratory, Oak Ridge, Tennessee 37831, USA. [3] Department of Physics and Astronomy, University of Tennessee, Knoxville, Tennessee 37996, USA. [4] Center for Nanophase Materials Sciences, Oak Ridge National Laboratory, Oak Ridge, Tennessee 37831, USA. [5] Computer Science and Mathematics Division, Oak Ridge National Laboratory, Oak Ridge, Tennessee 37831, USA. * These authors contributed equally to this work. † Present address: Department of Physics and Astronomy, University of Utah, Salt Lake City, Utah 84112, USA. Correspondence and requests for materials should be addressed to X.X. (email: xiaoshan.xu@unl.edu) or to J.S. (email: shenj5494@fudan.edu.cn).

Since the pioneering work by Dediu et al.[1] and Xiong et al.[2], many of the follow-up studies have focused on achieving high magnetoresistance (MR) in organic spin valves (OSVs) and uncovering the underlying transport mechanisms[3–11]. It has been generally acknowledged that the interfaces between the organic layer and the ferromagnetic electrodes play a critical role in determining the actual spin-dependent transport mechanism[12–15]. Barraud et al.[16] studied the spin transport of an OSV in which the thin organic layer serves as a tunnelling barrier as opposed to a diffusive spacer. A spin transport model describing the role of interfacial spin-dependent metal/organic hybridization on the amplitude and sign of the MR was put forward[16,17]. Recently, Schulz et al.[18] observed a reversal of the spin polarization of extracted charge carriers by introducing a thin interfacial permanent dipolar layer (LiF). This work indicates that the local electric dipole moment at the interface is important for MR, although in such a device the added dipolar layer plays only a passive role in terms of controlling MR.

In the following, we employ a ferroelectric (FE) thin interfacial layer between the organic semiconductor and the ferromagnetic electrode in OSV to achieve active control of MR. The material of choice for the FE layer is $PbZr_{0.2}Ti_{0.8}O_3$ (PZT), which has a large polarization ($\sim 80\,\mu C\,cm^{-2}$)[19]. The PZT layer can induce strong interfacial dipoles and built-in electric field between the organic spacer layer and the ferromagnetic electrode. The interfacial dipole is switchable by external electric field, potentially allowing the control of the spin polarization of injected carriers in organic spintronics. We show that the resistance can be controlled by not only the spin alignment of the two ferromagnetic electrodes[3], but also by the electric polarization of the PZT layer. The sign of MR changes when electric polarization of the PZT layer is reversed. This new tunability can be understood in terms of the change of relative energy level alignment between ferromagnetic electrode and the organic spacer caused by the electric dipole moment of the FE layer.

Results

Device structure and characterizations of the PZT films. Our fabricated OSVs consist a 65-nm Alq_3 (tris-(8-hydroxyquinoline) aluminum) layer sandwiched between a 5-nm-thick PZT layer epitaxially grown on a 30-nm-thick $La_{0.67}Sr_{0.33}MnO_3$ (LSMO) film-buffered $SrTiO_3$ (STO) substrate, and a 10-nm-thick (nominal thickness) cobalt layer with gold capping. In this $LSMO/PZT/Alq_3/Co$ junction (FE-OSV), Co and LSMO serve as the top and bottom magnetic electrodes, respectively. The device structure is schematically shown in Fig. 1a. As discussed in the following, such kind of devices exhibit striking tunability, that is, both the amplitude and sign of MR are tunable due to the presence of the FE PZT.

After epitaxial growth of PZT on LSMO/STO, the PZT layer has a smooth surface with atomically flat terraces, as characterized by atomic force microscopy shown in Fig. 1b. This provides an ideal base for preparing a well-defined Alq_3/PZT interface. The purpose of introducing the 5-nm-thick-PZT is to tune the energy level alignment between the Alq_3 and LSMO layers because the polarization in PZT is switchable by applying an electric field. Therefore, the polarization reversal of the PZT is crucial. Here we have characterized the polarization reversal of the PZT films used in the FE-OSV devices with piezoelectric force microscopy (PFM). Figure 1c shows a PFM image of the PZT film with a part of the film poled by a conducting tip with $\pm 2.5\,V$ relative to the LSMO bottom electrode. It shows that the polarization of the as-grown films is pointing 'up', and a clear reversal of polarization between 'up' and 'down' states can be created by sign reversal of the applied voltage. Figure 1d shows the voltage dependence of
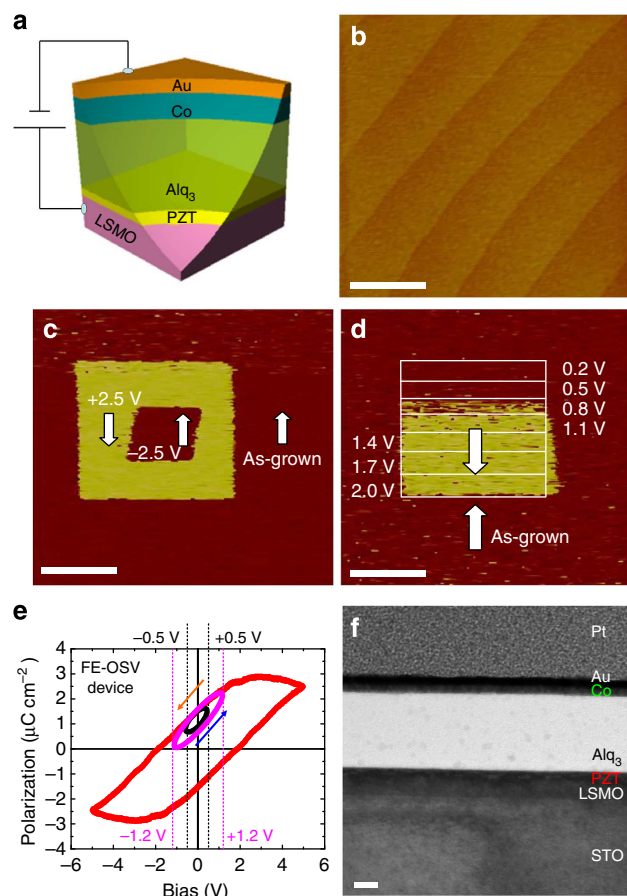

Figure 1 | Structure of the organic spin valves and characterization of ferroelectricity in the epitaxial PZT. (**a**) Schematic structure of a Au/Co/Alq_3/PZT/LSMO organic spin valve (FE-OSV). (**b**) Atomic force microscopy topography image of a PZT layer (5 nm in thickness) epitaxially grown on a LSMO (30 nm)/STO substrate. (**c**) PFM (phase) response measured after successively switching the polarization of the PZT film by applying $+2.5\,V$ and $-2.5\,V$ on the tip with respective to the LSMO bottom electrode. Note that the protocol of voltage polarity is different in PFM measurements from that in resistance measurements. (**d**) PFM image showing the polarization reversal by gradually increasing the applied voltage. The 'up' ('down') arrow corresponds to the polarization pointing out of (into) the film surface. Scale bar, 500 nm (**b**–**d**). (**e**) A typical polarization-voltage loop for the FE-OSV (device A). The black and pink circles illustrate the 'minor loops' corresponding to V_{MAX} of ± 0.5 and $\pm 1.2\,V$, respectively. The orange (blue) arrow indicates the direction of the ramp voltage: sweeping down (up) before the MR scans. (**f**) TEM image for FE-OSV device. Different layers can be distinguished as labelled. Scale bar, 20 nm.

the polarization. It is clear that the polarization of the PZT film (5 nm in thickness) starts to switch to the 'down' state when the voltage of the scanning probe exceeds 0.8 V. The polarization reversal of the PZT in the FE-OSV is characterized by the measurements of the hysteretic polarization-voltage dependence. As shown in Fig. 1e, with the Alq_3/Co/Au layers on top of PZT, the coercive voltage is $\sim 2\,V$. Figure 1f shows the transmission electron microscope (TEM) image for the cross-section of the FE-OSV. No significant diffusion of Co atoms into the Alq_3 layer is observed (see Supplementary Fig. 1 and Supplementary Note 1).

Hysteretic behaviour of the MR. It has been known that MR depends sensitively on the measuring voltage (V_{MR}). Previous

studies indicated that MR of LSMO/Alq$_3$/Co junctions (LSMO-OSV) increases with decreasing V_{MR}, reaching a maximum when V_{MR} is close to zero[2,16]. For our FE-OSV junctions, its MR depends not only on V_{MR}, but also on the history of the voltage applied, giving rise to a strong hysteretic behaviour. We characterize this hysteretic behaviour by measuring MR (V_{MR}) profile after applying a ramping voltage (V_{MAX}) that is larger than V_{MR} (see Supplementary Fig. 2 and Supplementary Note 2 for the detailed measurement protocol).

As shown in Fig. 2, for a FE-OSV containing an as-grown PZT layer, the MR (at $T = 11$ K) is always negative and is the largest when V_{MR} is near zero, which is similar to numerous previous studies on LSMO-OSV[2,4–6,8–11]. The different features in the FE-OSV are: (1) the MR(V_{MR}) profile is strongly affected by the initial voltage (V_{MAX}) and (2) a positive (negative) V_{MAX} leads to a negative (positive) shift of the MR(V_{MR}) profile along the V_{MR} axis (Fig. 2d,e). This shift (ΔV) is closely tied to the hysteretic behaviour of the PZT layer (so-called minor loops, see Fig. 1e) and increases with increasing V_{MAX}, as shown in Fig. 2f. The switching fields, MR uncertainty and MR loops reproducibility in FE-OSVs are shown in Supplementary Figs 3–5 and Supplementary Notes 3 and 4, respectively.

The hysteretic behaviour of the MR was not observed in OSVs without the FE layer, including a conventional LSMO/Alq$_3$/Co OSV (LSMO-OSV) and a LSMO/STO/Alq$_3$/Co OSV (STO-OSV) in which the 5-nm PZT is replaced by 5-nm STO (see Supplementary Figs 6 and 7, and Supplementary Note 5 for detailed MR loops and MR (V_{MR}) profiles). This indicates that the hysteretic behaviour of the MR in FE-OSV is tied to the presence of PZT. The distinctly different behaviour between the FE-OSV and the PZT-free OSVs (LSMO-OSV and STO-OSV) also allow us to exclude the possibility of resistive bistability mechanism caused by the existence of the trap states or current conduct path inside the Alq$_3$ layer[20,21], as otherwise similar MR behaviour

should be observed in both types of devices. We have also performed measurements on a LSMO/PZT/Co magnetic tunnel junction (FE-MTJ, see Supplementary Fig. 8). Although V_{MAX}
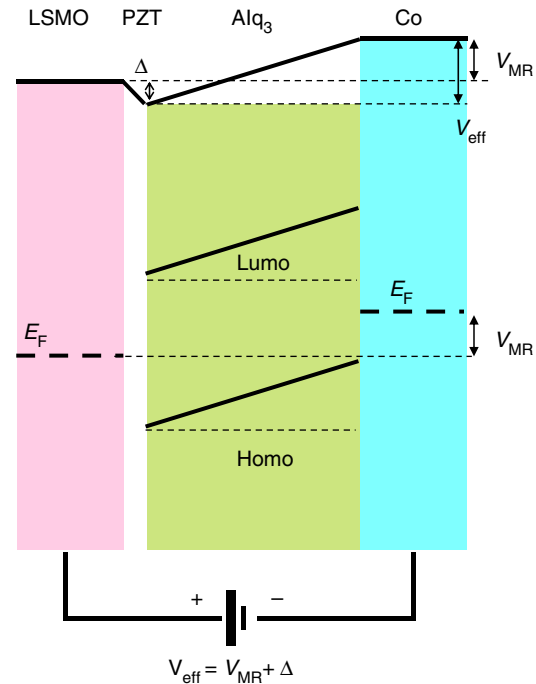

Figure 3 | Model of the hysteretic behaviour in FE-OSV. The relation between the effective bias on the spacer Alq$_3$ (V_{eff}), the applied bias at measurement (V_{MR}) and the vacuum level shift (Δ) by the remanent dipole moments of the FE PZT layer, is $V_{eff} = V_{MR} + \Delta$.
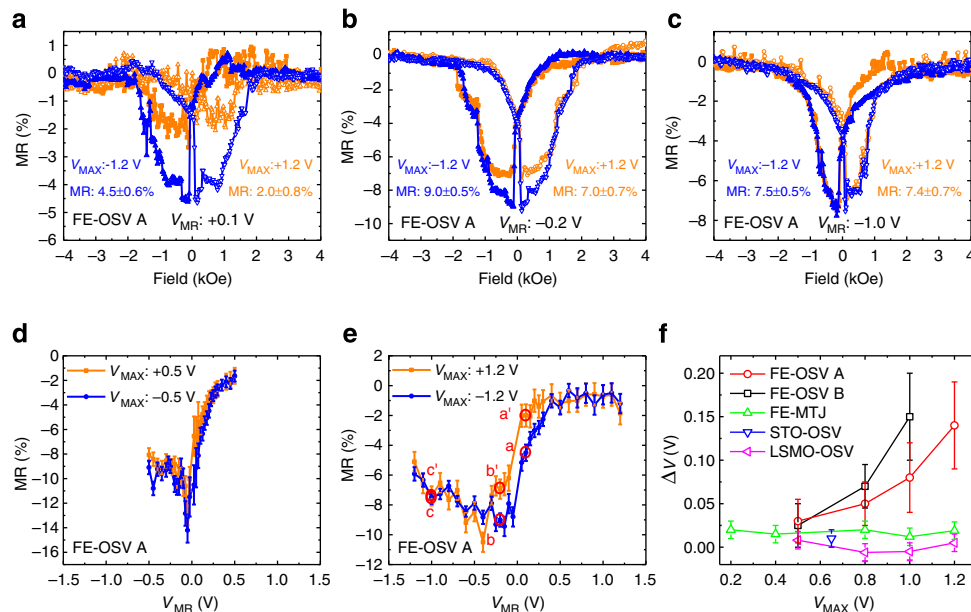

Figure 2 | Hysteretic behaviour of the MR at $T = 11$ K. (a–c) MR scans in the as-grown state of a FE-OSV device (PZT in 'up' polarization) with the same applied bias (V_{MR}) but different initial ramping voltage (V_{MAX}). Here, LSMO is treated as the anode. The switching fields of FE-OSV are confirmed by superconducting quantum interference device measurements (see Supplementary Fig. 3 and Supplementary Note 3). (d,e) MR(V_{MR}) profiles taken at two different values of positive (orange) and negative (blue) V_{MAX}. ΔV represents the shift of MR (V_{MR}) profiles, and a'/a, b'/b and c'/c mark the positions at which the six MR loops in a–c are taken(V_{MAX}: $+1.2$ V and -1.2 V). (f) Dependence of ΔV on V_{MAX}. ΔV for both FE-OSV devices (A and B) increases with increasing V_{MAX}, while the three types of control devices (FE-MTJ, STO-OSV and LSMO-OSV) do not show any significant ΔV. The error bars represent the uncertainty of the MR measurements including both systematic error (estimated from the asymmetry in the MR loops) and the statistical error (see Supplementary Fig. 4 and Supplementary Note 4).

affects the MR (V_{MR}) profile, which confirms the results of Pantel *et al.*[22] and Valencia *et al.*[23], it does not induce any shift of the MR (V_{MR}) profile along the V_{MR} axis. The comparison of the MR (V_{MR}) profiles of the FE-OSV and the FE-MTJ suggests that the effective voltage generated by the dipole of the PZT (instead of the interfacial bonding) is responsible for the hysteretic behaviour of the MR in the FE-OSV. The FE-MTJ does not show hysteretic behaviour of MR, because no direct dipole exists on the surface of the PZT due to the screening effect from the two metal electrodes in direct contact with the PZT layer.

A schematic model is illustrated in Fig. 3 to explain this hysteretic behaviour of MR in the FE-OSV. When a V_{MAX} is applied to the junction, the polarization of the PZT gets modified. Owing to the dipole moment created by the electric polarization of PZT, the effective voltage V_{eff} applied on the Alq$_3$ layer equals $V_{MR} + \Delta$, where Δ is the vacuum level shift caused by the remnant dipole moment of PZT. When a positive (negative) V_{MAX} is applied, Δ becomes larger (smaller), which explains why the MR (V_{MR}) profile can be shifted by V_{MAX}.

Switch of the MR sign. Remarkably, a reversal of the polarization of the PZT layer leads to a sign change of the MR in the FE-OSV. After measuring the MR and MR (V_{MR}) profile (Fig. 4a–c) for the FE-OSV device B (PZT layer in the as-grown state), we measured

polarization-voltage dependence up to ± 5 V. The measurement ended at -5.0 V to pole the PZT to the 'down' state. The MR measurements of the FE-OSV device after this treatment are shown in Fig. 4d,e,g,h. The shape of the MR (V_{MR}) profile changes dramatically, as shown in Fig. 4i. In particular, the sign of the MR changes from negative (Fig. 4a,b) to positive (Fig. 4d,g,h) for a certain range of V_{MR}. A close correlation between the polarization of PZT and the sign of the MR can be identified by comparing the hysteretic behaviour of the MR (V_{MR}) profile and the possible minor polarization-voltage loop of the PZT, as illustrated in Fig. 4f, that is, when the polarization of PZT is negative enough (more 'down' state), the MR becomes positive.

The physical origin of MR sign of the LSMO/Alq$_3$/Co junctions has been studied previously by Barraud *et al.* using nanoindentation-based devices. It was argued that first, the spin polarization alignment P^* at the Co/Alq$_3$ interface is positive when electrons move from Co to Alq$_3$, that is, $P^*(Alq_3 \rightarrow Co) > 0$ where the arrow indicates the direction of the electric current[4,24]; second, the density of states for Alq$_3$ at the Alq$_3$/LSMO interface is spin polarized due to the coupling between the two materials, causing $P^*(LSMO \rightarrow Alq_3) < 0$ when the Alq$_3$ serves as a diffusive spacer. Following these arguments, Barraud *et al.*[16] concluded that the sign of MR at small measurement voltages is determined by the sign of the product of $P^*(Alq_3 \rightarrow Co)$ and $P^*(LSMO \rightarrow Alq_3)$; the result is negative. In the FE-OSV studied here, the
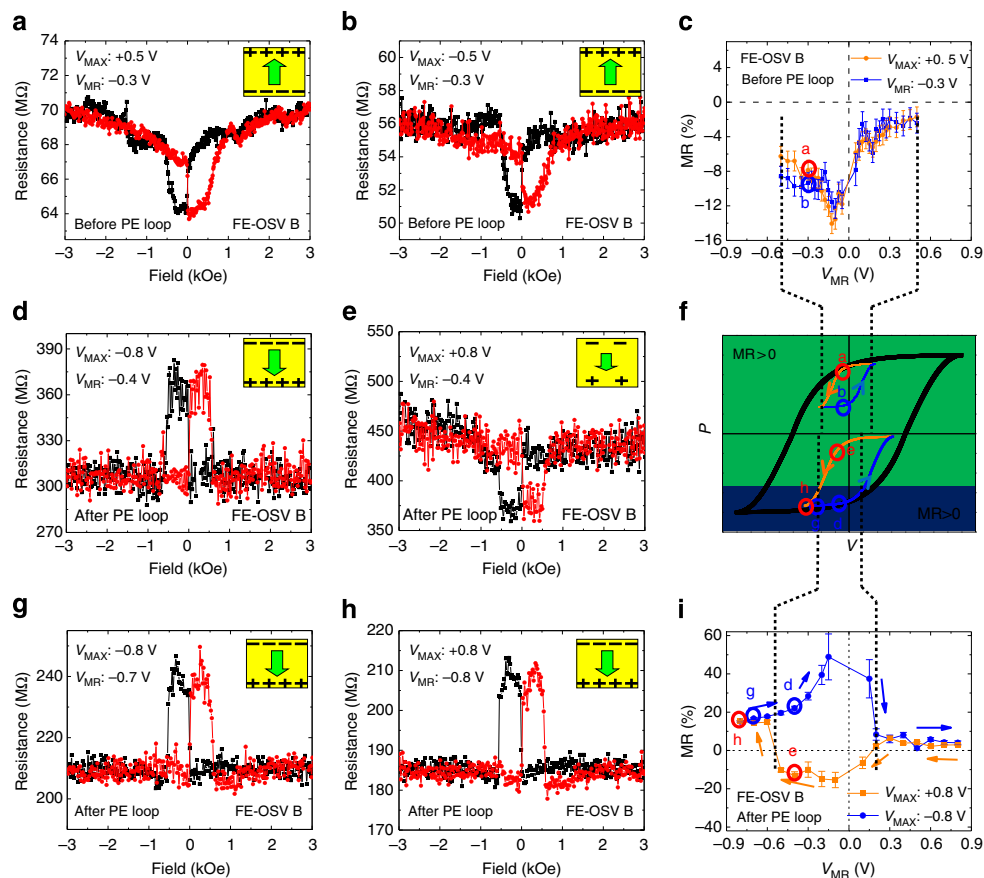

Figure 4 | Reversal of MR sign at T = 11 K. (a,b) MR scans for the 'as-grown' state of the FE-OSV device B acquired at $V_{MR} = -0.3$ V/$V_{MAX} = +0.5$ V and $V_{MR} = -0.3$ V/$V_{MAX} = -0.5$ V, respectively. **(c)** MR (V_{MR}) profiles at $V_{MAX} = +0.5$ V (orange) and -0.5 V (blue). **(d,e,g,h)** MR scans taken when the polarization of the PZT is reversed. **(f)** Comparison of the MR (V_{MR}) profile and the polarization-voltage loop, illustrating the correlation between the sign of MR and the polarization of the PZT. The asymmetric regions of MR < 0 and MR > 0 in polarization-voltage loop indicate that the reversal of MR only occurs at higher degree of polarization in the 'down' state of PZT. **(i)** MR(V_{MR}) profiles at V_{MAX}: ± 0.8 V when the polarization of the PZT is reversed. The red (blue) circles indicate the V_{MR} values at which the MR loops (**a,b,d,e,g,h**) are taken with positive (negative) V_{MAX}. The error bars are estimates using the same analysis as that in Fig. 2.

$P^*(\text{Alq}_3 \rightarrow \text{Co}) > 0$ can be assumed similarly; the polarization alignment P^* between LSMO and Alq_3 is not changed by inserting a thin layer (5 nm) of as-grown PZT or STO, but can be changed by poling the PZT layer, according to the behaviour of the observed MR. This novel feature in FE-OSV must be due to the more complex $\text{LSMO/PZT} \rightarrow \text{Alq}_3$ interface. We propose the following model based on the relative energy level alignment between Alq_3 and LSMO to understand the switching of MR sign in FE-OSV.

Here we consider mainly the hole transport, because for Alq_3 the energy difference between the highest occupied molecular orbital (HOMO) and Fermi levels of the two metallic LSMO and Co electrodes are much smaller than that between the lowest unoccupied molecular orbital and the Fermi levels[2,18,25]. As shown in Fig. 5a, when the polarization of the PZT layer is pointing 'up' (the as-grown state) or zero (the same case as for STO), the hole injection from the LSMO electrode for positive V_{MR} is from the Fermi level (which lies in the spin majority band) of LSMO to the HOMO of Alq_3, which is the same as in the LSMO-OSV. Therefore, $P^*(\text{LSMO/PZT} \rightarrow \text{Alq}_3) < 0$, corresponding to a negative MR considering $P^*(\text{Alq}_3 \rightarrow \text{Co}) > 0$ as discussed above[2,4]. When the polarization of the PZT layer is pointing 'down', the HOMO of Alq_3 is shifted up due to the dipole moment of PZT. Therefore, another state of the LSMO with opposite spin polarization may be accessible (Fig. 5b). Hence, $P^*(\text{LSMO/PZT} \rightarrow \text{Alq}_3)$ changes the sign and becomes positive, corresponding to a reversed, positive MR.

Our proposed model relies on two key assumptions: (1) the dipole moment of the PZT layer shifts the Alq_3 HOMO level and (2) the shift of the Alq_3 HOMO level results in a shift of the initial state of LSMO for the hole injection between energy band of opposite spin polarizations. The first assumption was used by Schultz et al.[18] to explain the MR sign reversal in a $\text{FeCo/Alq}_3/\text{LiF/NiFe}$ junction by proposing a shift of the HOMO of Alq_3 due

to the dipole moment of LiF layer. The second assumption can be justified by the half metallicity of LSMO. As illustrated in Fig. 5, the conduction band of LSMO splits into spin majority and minority bands due to the exchange interaction, causing half metallicity because the Fermi level lies within the fully polarized spin majority band[26–28]. Therefore, when the HOMO of Alq_3 is shifted up due to the reversal of dipole moment of PZT, the initial state of LSMO for hole injection may change to spin minority band with opposite spin polarization. Note that this reversed dipole moment of PZT needs to be large enough to shift the HOMO level of Alq_3 to 'reach' the spin minority band of LSMO and obtain reversed positive MR values. Otherwise, only negative MR values will be observed, as shown in Fig. 4f (also see Supplementary Fig. 9 and Supplementary Note 6).

Besides changing the energy level alignments, switching the electric polarization of the FE layer may also modify the coupling between the FE layer and the magnetic electrode, depending on the detailed electronic structure of the electrode and the nature of the electric polarization of the FE material[29–31]. These effects may also change the spin polarization at the interface between the FE material and the metal electrode[22,23,31]. However, both the magnetic structure of the LSMO and the spin polarization of the PZT are not expected to be affected very much by the electric polarization of the PZT, because of the robust magnetic properties of the $\text{La}_{0.7}\text{Sr}_{0.3}\text{MnO}_3$ with given composition (far from the metal-insulator phase boundary) and the large distance between the Mn site from LSMO and Ti sites from PZT at the interface[22,23,30,31].

Another possible scenario involves the change of carrier type when the energy level alignment between LSMO and Alq_3 is changed: the carriers take the path of the HOMO (lowest occupied molecular orbital), that is, hole (electron) transport in Alq_3 when the energy levels of Alq_3 is shifted 'down' ('up') due to the 'up' ('down') polarization of the PZT layer. This, however, contradicts our experimental observations because in the FE-OSV with the as-grown ('up' polarization) PZT, the MR is negative, the same as that in the STO-OSV or LSMO-OSV without any interfacial layers, suggesting that the carrier type in FE-OSV is most probably holes instead of electrons[18,25], as in the STO-OSV or LSMO-OSV.

Discussion

The active control of the energy level alignment between the electrodes and the organic material, manifested here in the active control of the MR, not only carries promises for multistate control of organic spin-valve devices, but will also impact other organic electronic devices, in particular those applied in photovoltaics and solid-state lighting. Specifically, the charge carrier injection efficiency of the organic light emitting diode is determined by the relative alignment between the Fermi energy of the electrode and the energy levels of the organic material[32]. The charge collection efficiency in an organic photovoltaic device also depends on the alignment of the energy levels of the acceptor organic material and the electrode[33]. Therefore, the realization of the active control of the level alignment using an FE interfacial layer demonstrated in this letter may also lead to successful optimization of other organic electronic devices by tailoring the energy landscape of the comprising materials using a tunable interfacial layer.
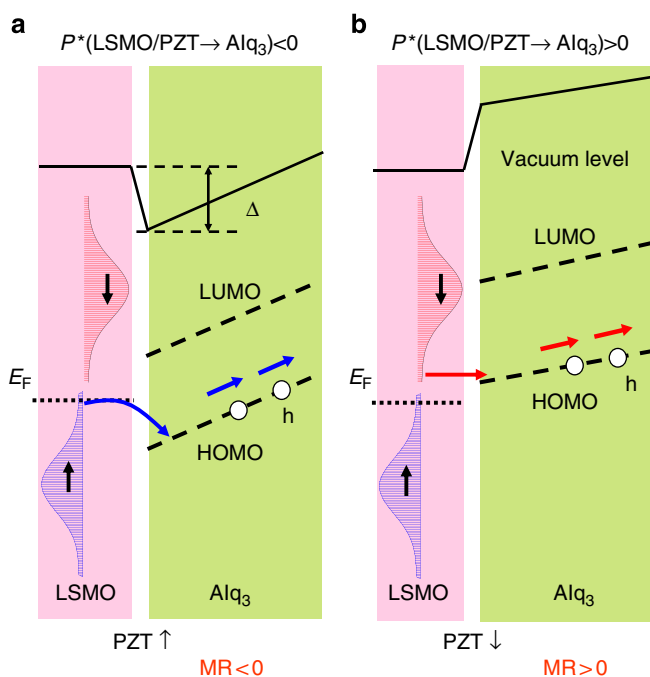

Figure 5 | Model of MR sign reversal in FE-OSV. (a,b) The energy diagrams of the FE-OSV device when the electric polarization of the PZT is 'up' and 'down', respectively. The white circles represent the injected holes in the device. The blue (red) arrows indicate the injection of spin-polarized holes from the majority (minority) band of LSMO.

Methods

pressure of 5.0×10^{-9} Torr. Without breaking the vacuum, the Co (10 nm)/Au (7 nm) was then deposited by thermal evaporation at substrate temperature of 280 K to complete the formation of the top electrode in a crossbar configuration through the shadow mask. The thickness of layers were controlled by a quartz thickness monitor. The device area is $\sim 200\,\mu m \times 50\,\mu m$.

Device characterizations. Atomic force microscopy topography images and PFM were taken using a Veeco Dimension 3100 at room temperature. The TEM samples were prepared by a FEI Dual-beam (Focus-Ion-Beam/SEM) system, and high-resolution TEM images were taken by a FEI Tecnai transmission electric microscope with beam energy of 200 kV. Radiant Premier II FE measuring system was used to detect the polarization-voltage loops of the devices at 50 Hz. Magnetometer measurements were carried out using a Quantum Design superconducting quantum interference device system. Magnetic fields were applied in the plane of the thin film. Transport measurements were carried out using a Quantum Design Physical Property Measurement System (PPMS) combined with a Keithley 2400 source meter at $T = 11$ K. Magnetic fields were applied in the plane of the thin film. The MR is defined as: $MR = (R_{antiparallel} - R_{parallel})/R_{parallel}$, where $R_{antiparallel}$ is the junction resistance in the antiparallel magnetic configuration and $R_{parallel}$ is the resistance at the parallel configuration. The detailed MR measurement protocols are shown in Supplementary Fig. 2 and Supplementary Note 2.

References

1. Dediu, V., Murgia, M., Matacotta, F. C., Taliani, C. & Barbanera, S. Room temperature spin polarized injection in organic semiconductor. *Solid State Commun.* **122**, 181–184 (2002).
2. Xiong, Z. H., Wu, D., Vardeny, Z. V. & Shi, J. Giant magnetoresistance in organic spin-valves. *Nature* **427**, 821–824 (2004).
3. Fert, A. Nobel Lecture: Origin, development, and future of spintronics. *Rev. Mod. Phys.* **80**, 1517–1530 (2008).
4. Dediu, V. et al. Room-temperature spintronic effects in Alq₃-based hybrid devices. *Phys. Rev. B* **78**, 115203 (2008).
5. Dediu, V. A., Hueso, L. E., Bergenti, I. & Taliani, C. Spin routes in organic semiconductors. *Nat. Mater.* **8**, 707–716 (2009).
6. Wang, F. & Vardeny, Z. V. Recent advances in organic spin-valve devices. *Synth. Met.* **160**, 210–215 (2010).
7. Schoonus, J. J. et al. Magnetoresistance in hybrid organic spin valves at the onset of multiple-step tunneling. *Phys. Rev. Lett.* **103**, 146601 (2009).
8. Nguyen, T. D. et al. Isotope effect in spin response of π-conjugated polymer films and devices. *Nat. Mater.* **9**, 345–352 (2010).
9. Drew, A. J. et al. Direct measurement of the electronic spin diffusion length in a fully functional organic spin valve by low-energy muon spin rotation. *Nat. Mater.* **8**, 109–114 (2009).
10. Cinchetti, M. et al. Determination of spin injection and transport in a ferromagnet/organic semiconductor heterojunction by two-photon photoemission. *Nat. Mater.* **8**, 115–119 (2009).
11. Sun, D. et al. Giant magnetoresistance in organic spin valves. *Phys. Rev. Lett.* **104**, 236602 (2010).
12. Zhan, Y. Q. et al. The role of aluminum oxide buffer layer in organic spin-valves performance. *Appl. Phys. Lett.* **94**, 53301–53303 (2009).
13. Zhan, Y. Q. et al. Energy level alignment and chemical interaction at Alq₃/Co interfaces for organic spintronic devices. *Phys. Rev. B* **78**, 45208 (2008).
14. Grobosch, M., Dorr, K., Gangineni, R. B. & Knupfer, M. Energy level alignment and injection barriers at spin injection contacts between La₀.₇Sr₀.₃MnO₃ and organic semiconductors. *Appl. Phys. Lett.* **92**, 23302–23303 (2008).
15. Zhan, Y. Q. et al. Alignment of energy levels at the Alq₃/La₀.₇Sr₀.₃MnO₃ interface for organic spintronic devices. *Phys. Rev. B* **76**, 45406 (2007).
16. Barraud, C. et al. Unravelling the role of the interface for spin injection into organic semiconductors. *Nat. Phys.* **6**, 615–620 (2010).
17. Sanvito, S. Molecular spintronics: the rise of spinterface science. *Nat. Phys.* **6**, 562–564 (2010).
18. Schulz, L. et al. Engineering spin propagation across a hybrid organic/inorganic interface using a polar layer. *Nat. Mater.* **10**, 39–44 (2011).
19. Pacchioni, G. Two-dimensional oxides: multifunctional materials for advanced technologies. *Chem. A Eur. J.* **18**, 10144–10158 (2012).
20. Prezioso, M. et al. Electrically programmable magnetoresistance in multi-functional organic-based spin valve devices. *Adv. Mater.* **23**, 1371–1375 (2011).
21. Prezioso, M. et al. A single-device universal logic gate based on a magnetically enhanced memristor. *Adv. Mater.* **25**, 534–538 (2013).
22. Pantel, D., Goetze, S., Hesse, D. & Alexe, M. Reversible electrical switching of spin polarization in multiferroic tunnel junctions. *Nat. Mater.* **11**, 289–293 (2012).
23. Valencia, S. et al. Interface-induced room-temperature multiferroicity in BaTiO₃. *Nat. Mater.* **10**, 753–758 (2011).
24. Santos, T. S. et al. Room-temperature tunnel magnetoresistance and spin-polarized tunneling through an organic semiconductor barrier. *Phys. Rev. Lett.* **98**, 16601 (2007).
25. Nguyen, T. D., Ehrenfreund, E. & Vardeny, Z. V. Spin-polarized light-emitting diode based on an organic bipolar spin valve. *Science* **337**, 204–209 (2012).
26. Park, J.-H. et al. Direct evidence for a half-metallic ferromagnet. *Nature* **392**, 794–796 (1998).
27. Bowen, M. et al. Nearly total spin polarization in La₂/₃Sr₁/₃MnO₃ from tunneling experiments. *Appl. Phys. Lett.* **82**, 233–235 (2003).
28. Park, J.-H. et al. Magnetic properties at surface boundary of a half-metallic ferromagnet La₀.₇Sr₀.₃MnO₃. *Phys. Rev. Lett.* **81**, 1953–1956 (1998).
29. López-Encarnación, J. M., Burton, J. D., Tsymbal, E. Y. & Velev, J. P. Organic multiferroic tunnel junctions with ferroelectric poly(vinylidene fluoride) barriers. *Nano Lett.* **11**, 599–603 (2010).
30. Burton, J. D. & Tsymbal, E. Y. Prediction of electrically induced magnetic reconstruction at the manganite/ferroelectric interface. *Phys. Rev. B* **80**, 174406 (2009).
31. Gracia, V. et al. Ferroelectric control of spin polarization. *Science* **327**, 1106–1110 (2010).
32. Shen, Y., Hosseini, A. R., Wong, M. H. & Malliaras, G. G. How to make ohmic contacts to organic semiconductors. *ChemPhysChem* **5**, 16–25 (2004).
33. Yuan, Y. et al. Efficiency enhancement in organic solar cells with ferroelectric polymers. *Nat. Mater.* **10**, 296–302 (2011).
34. Lee, H. N. et al. Suppressed dependence of polarization on epitaxial strain in highly polar ferroelectrics. *Phys. Rev. Lett.* **98**, 217602 (2007).

Author contributions

D.S. and X.X. designed and supervised the experiments. D.S., M.F., X.X. and L.F. prepared the experimental setup. D.S. and M.F. carried out the transport measurement. M.F., D.S., H.G., Y.W. and W.Y. carried out the device preparations. M.F., Y.W. and W.Y. carried out the measurements of TEM imaging, PE loops and magnetic properties. L.J and H.N.L. were responsible for growing PZT, STO, LSMO films and PFM measurements. D.S., M.F., X.X, H.W., P.C.S., T.Z.W. and Z.G. carried out the data analysis. X.X. and X.G.Z. contributed to the theoretical modelling for the interpretation. J.S. was responsible for project planning, group managing and the final writing. All authors contributed to the physical understanding, data analysis and manuscript preparation.

Additional information

Supplementary Information accompanies this paper at http://www.nature.com/naturecommunications

Competing financial interests: The authors declare no competing financial interests.

Reprints and permission information is available online at http://npg.nature.com/reprintsandpermissions/

How to cite this article: Sun, D. et al. Active control of magnetoresistance of organic spin valves using ferroelectricity. *Nat. Commun.* 5:4396 doi: 10.1038/ncomms5396 (2014).
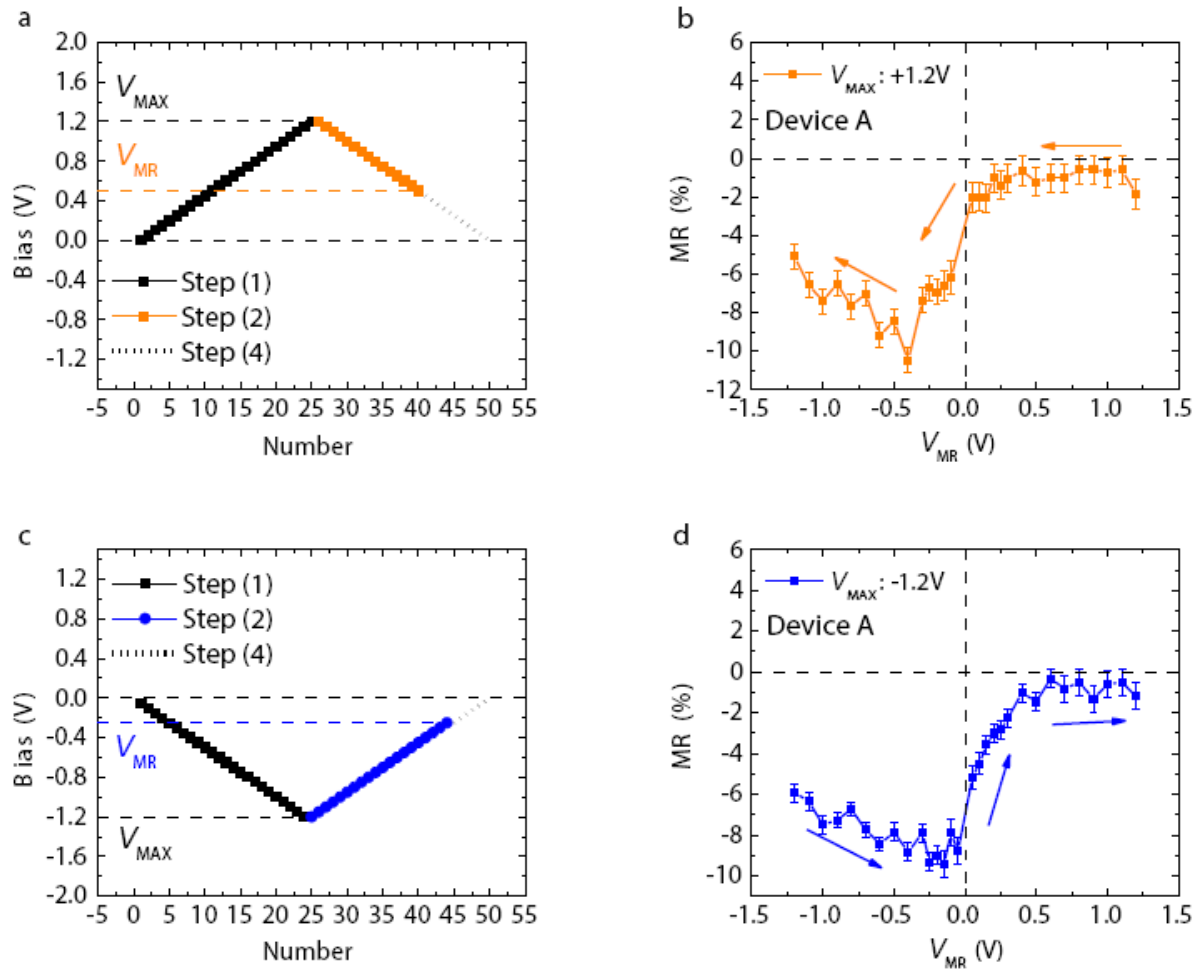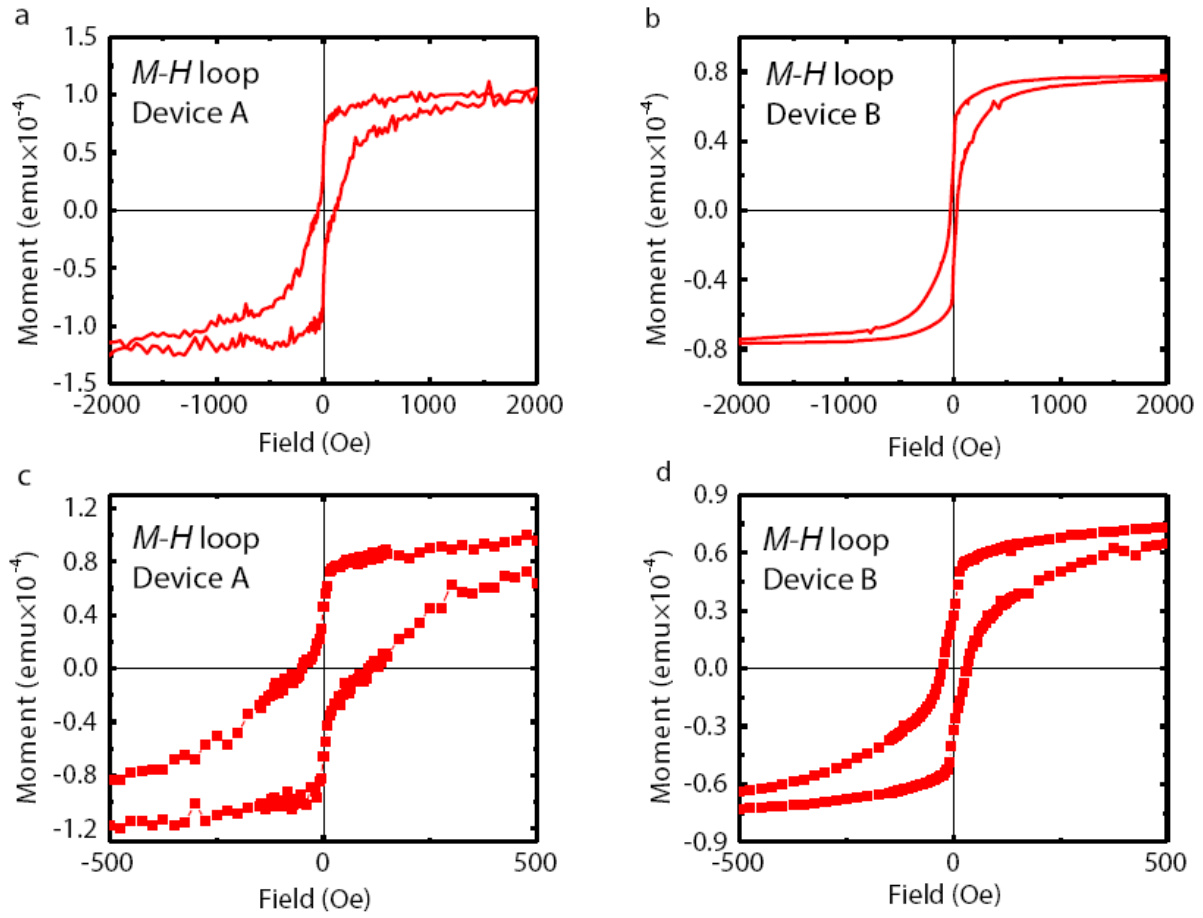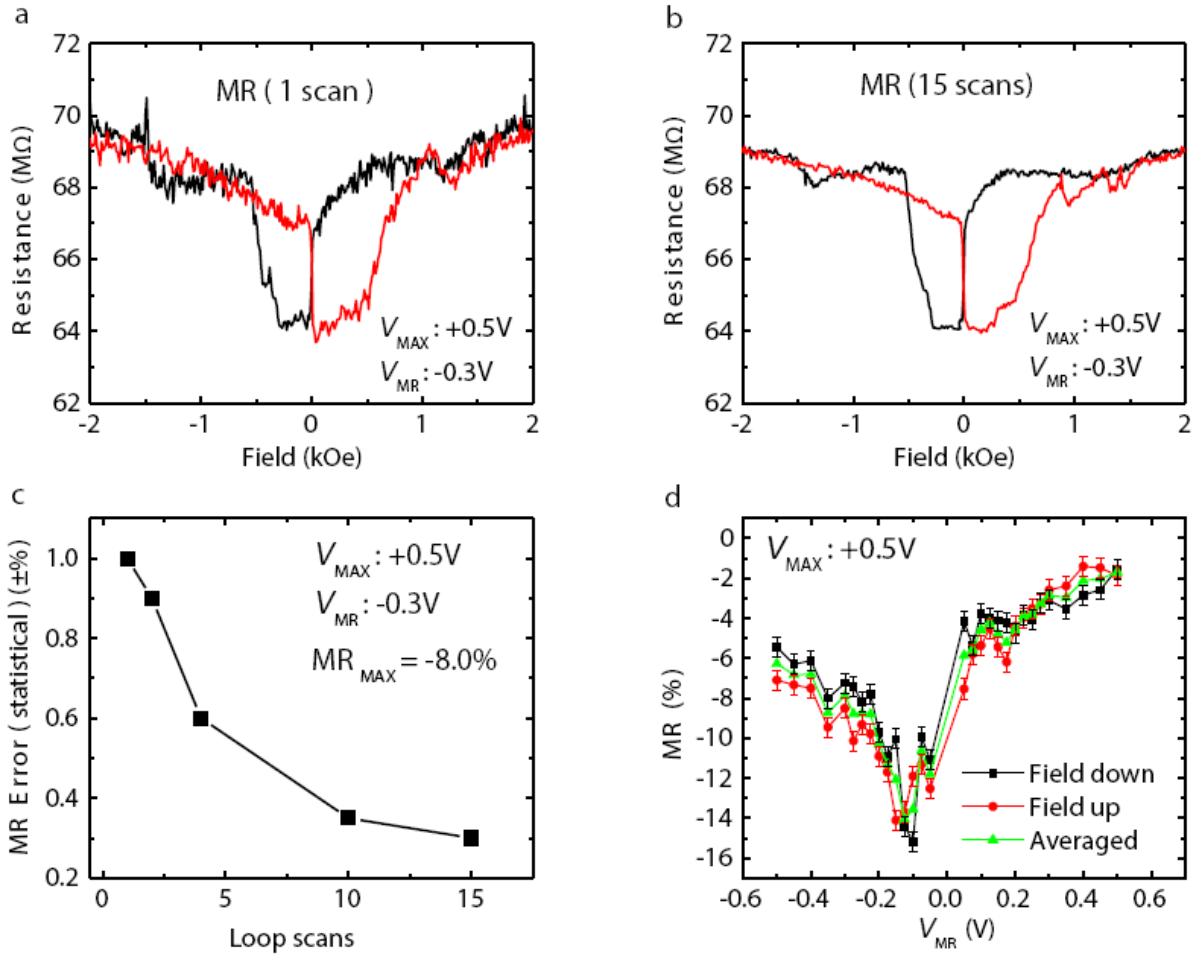
SUPPLEMENTARY FIGURES
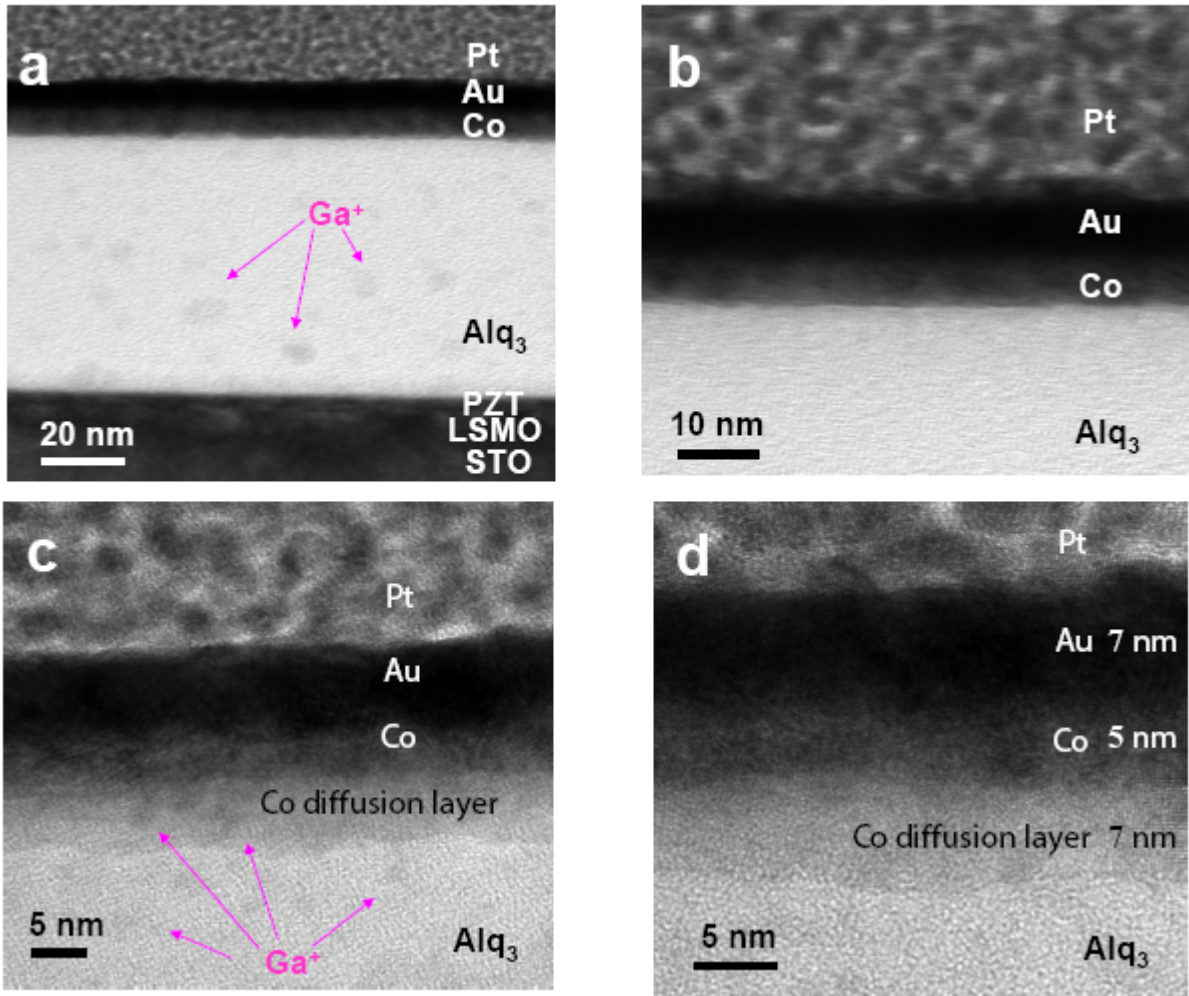
Supplementary Figure 1 | TEM images for FE-OSV. **a** to **d**, TEM images with different magnification. Only slight interdiffusion between Co and Alq$_3$ layer is observed. The random contaminations from "Ga$^+$" due to the focused ion beam (FIB) are marked, which exists in both Alq$_3$ layer and Co/Au electrodes.

Supplementary Figure 2 | Measurement protocol. a and **c** Ramping positive and negative bias list before taking the MR loops, respectively. V_{MR} is the bias when the ramping curve stops, followed by a $R(H)$ measurement at this bias. **b** and **d** MR (V_{MR}) profile according to two different ramping curves in **a** and **c**, respectively. The orange/ blue arrows present the sweeping direction of V_{MR}.

Supplementary Figure 3 | SQUID measurement. a and **c**, *M-H* loops for FE-OSV device A with two different magnetic field range (device in the **Fig. 2** of the main text). **b** and **d**, *M-H* loops for FE-OSV device B (device in the **Fig. 4** of the main text).

**Supplementary Figure 4 | MR uncertainty. a** and **b**, MR loops averaged over difference number of scans (V_{MAX}= +0.5V, V_{MR}= -0.3V, device B). **c**, Statistical MR uncertainty as a function of the number of scans. **d**, MR (V_{MR}) profiles with error bars representing the statistical uncertainty. MR values are calculated separately while magnetic field is ramping "down" (black) and "up" (red). The averaged values (green) are also shown in the figure; these averaged values are the MR values reported in the main text. The differences between the MRs measured when the field is ramping up and when the field is ramping down are taken as the systematic MR uncertainty.
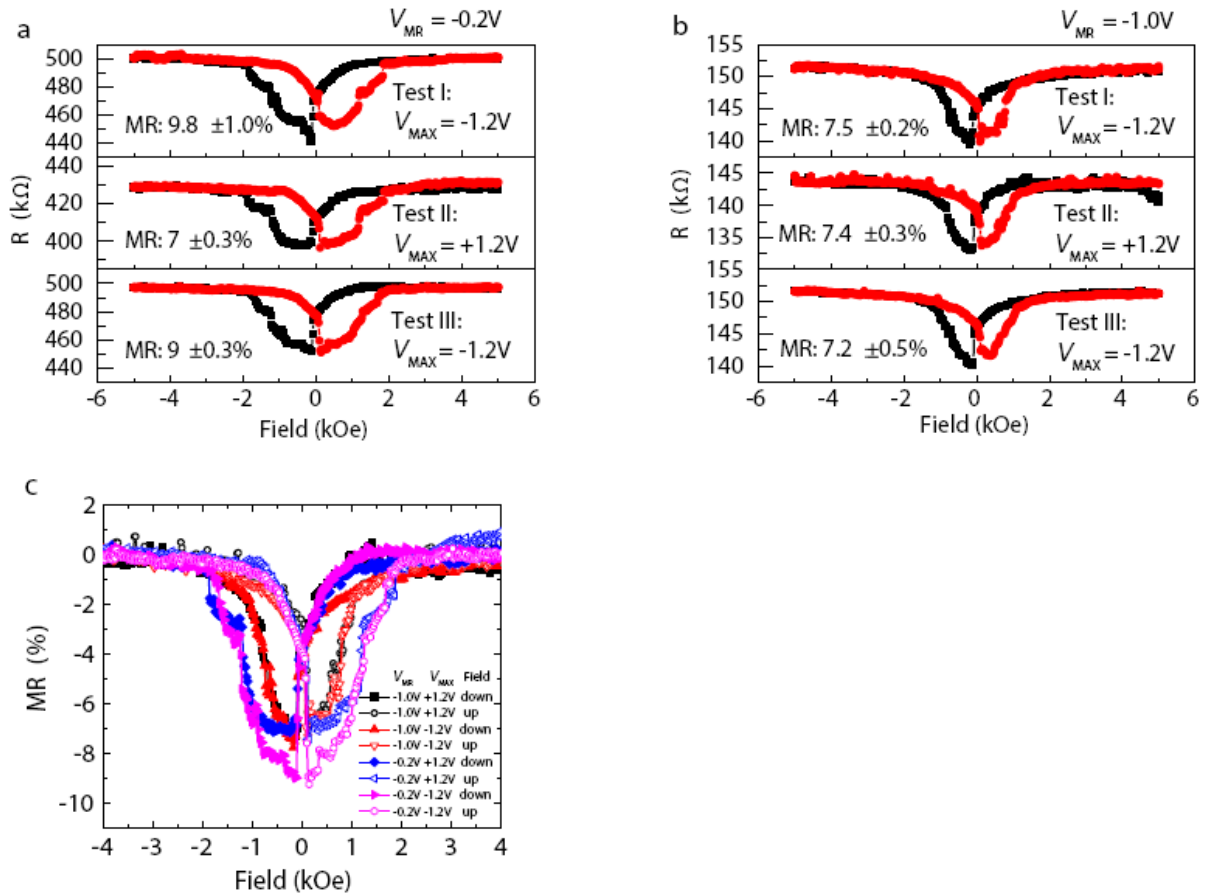
Supplementary Figure 5 | Reproducibility of the MR loops. a and **b**, Comparison of MR loops under the sequence of three ramp voltages (V_{MAX}: -1.2V, +1.2V and -1.2V) at V_{MR}= -0.2V and -1.0V, respectively (FE-OSV A). The resistance of the device is recovered to initial state after the sequence. **c**, Normalized MR loops for V_{MR}: -0.2V and -1.0V with V_{MAX}: +/- 1.2V. Note that the switching field for the same device does not changes under different ramp voltage process (both saturated at ~2 kOe), although the magnitude of MR is different.
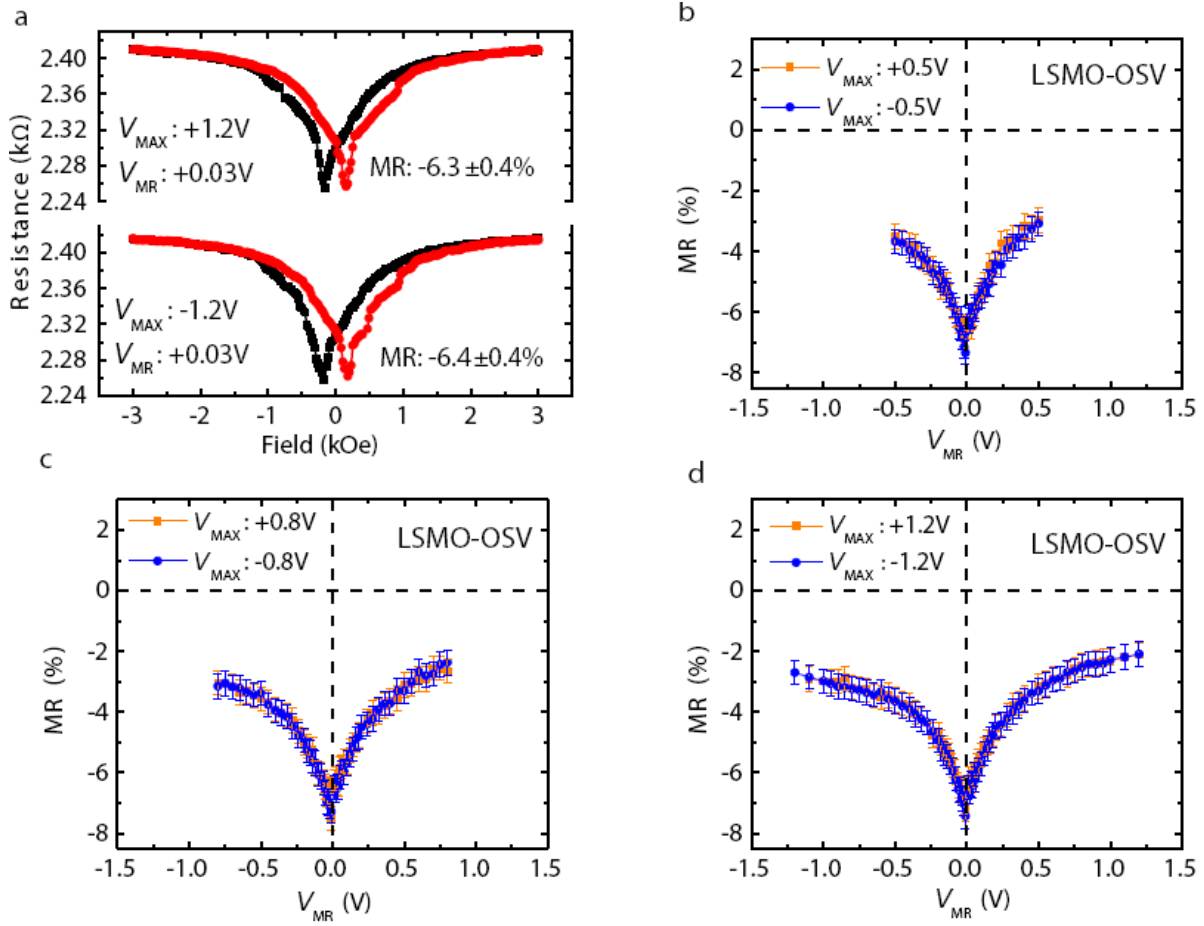
Supplementary Figure 6 | LSMO-OSV control device. a, MR loops of LSMO-OSV at the same bias voltage (V_{MR} = +0.03V) but with two different V_{MAX} (+/- 1.2V). **b** to **d**, MR(V_{MR}) profiles and the dependence on V_{MAX}. No hysteretic behavior of MR is observed in the device. The measurements were taken at T=11K.
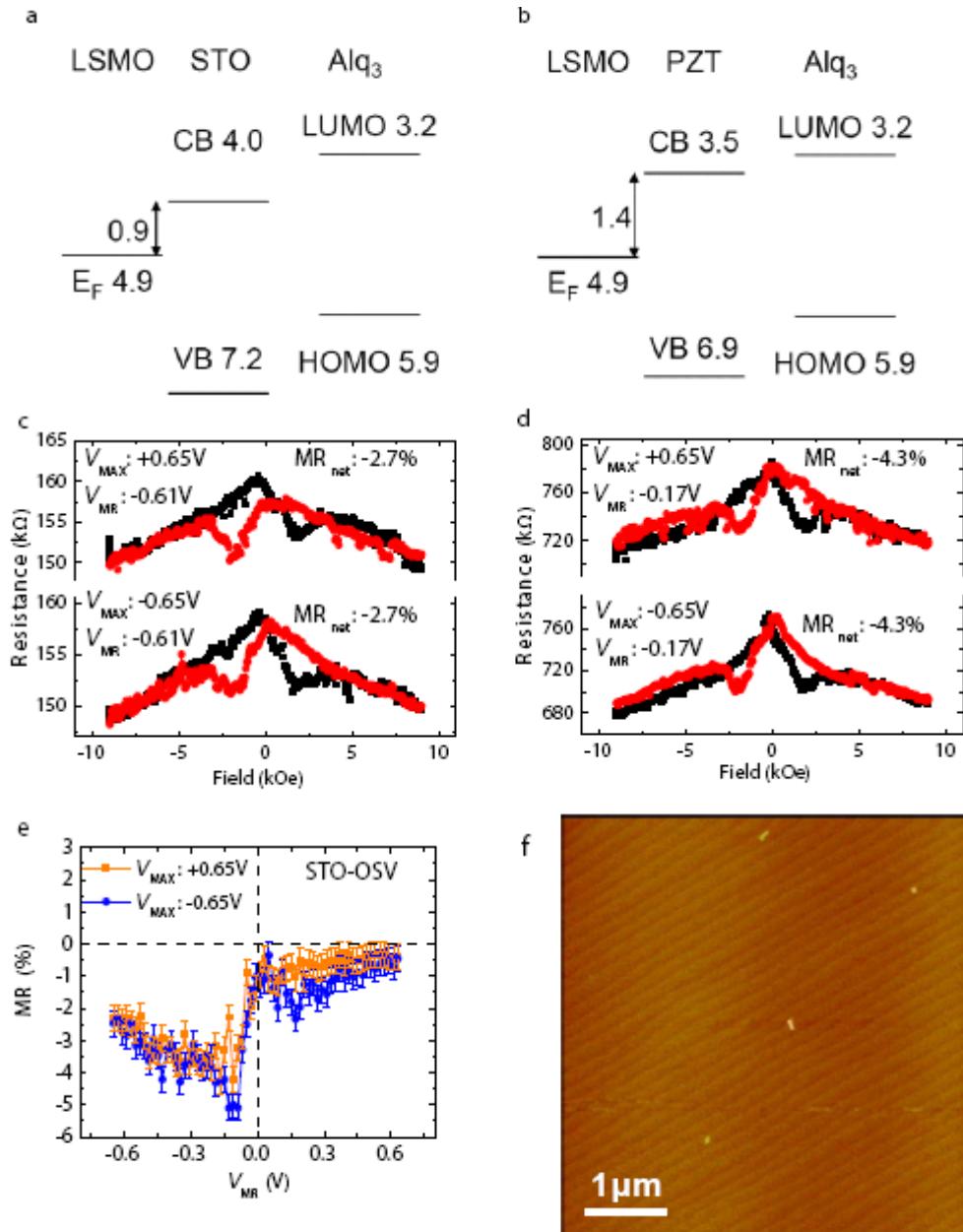
Supplementary Figure 7 | STO-OSV control device. a, Energy level diagram for LSMO/STO-OSV device. **b**, Energy level diagram for LSMO/PZT-OSV device (without dipoles). **c** and **d**, $R(H)$ dependence of STO-OSV device at V_{MR}=-0.61V and -0.17V, respectively. **e,** MR(V_{MR}) profiles of STO-OSV device. No shift of the profile is observed. The measurements were taken at T=11K. **f,** Surface of the 5 nm STO grown on 30 nm LSMO on STO substrate measured using atomic force microscope (5 μm × 5 μm); the clear atomic terrace indicates the flatness of the surface.
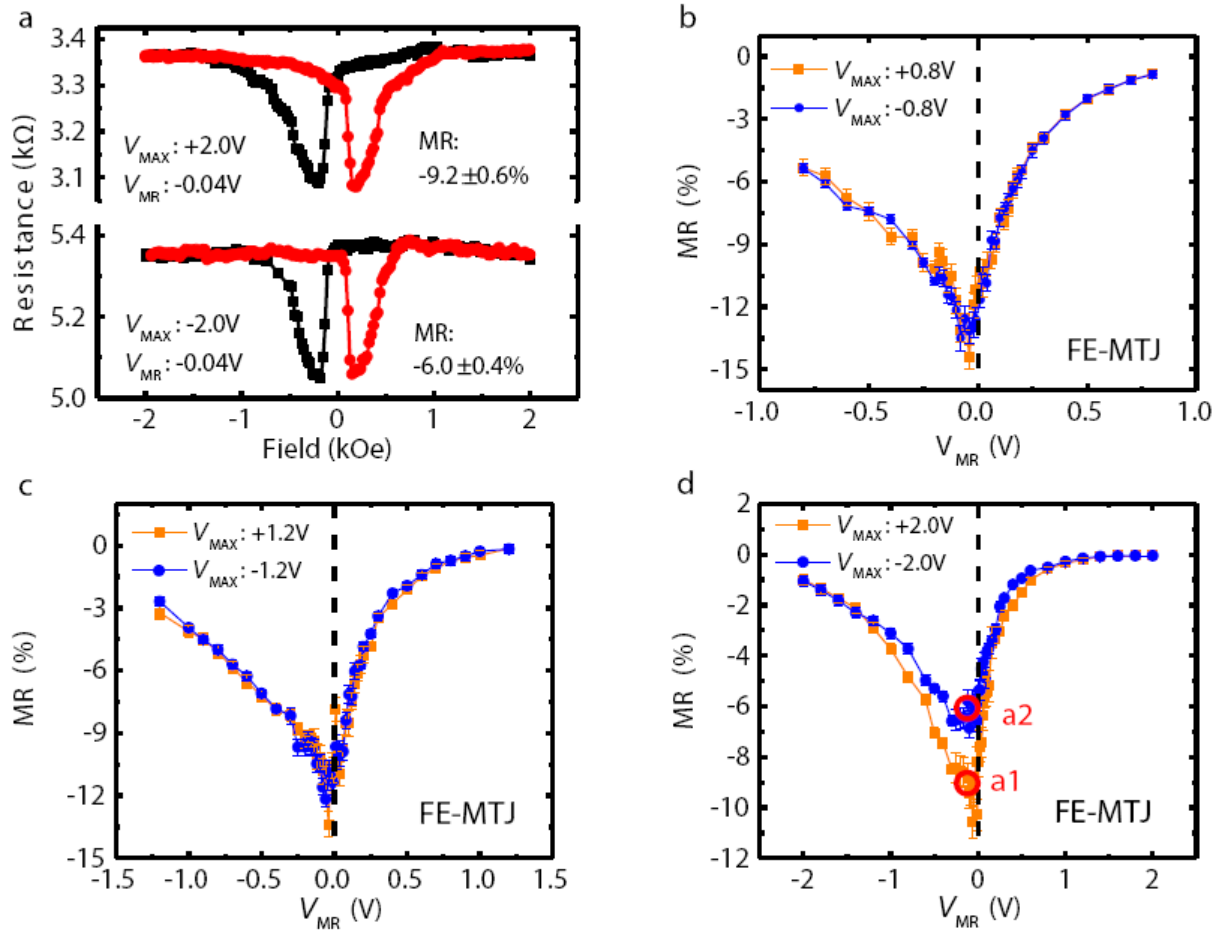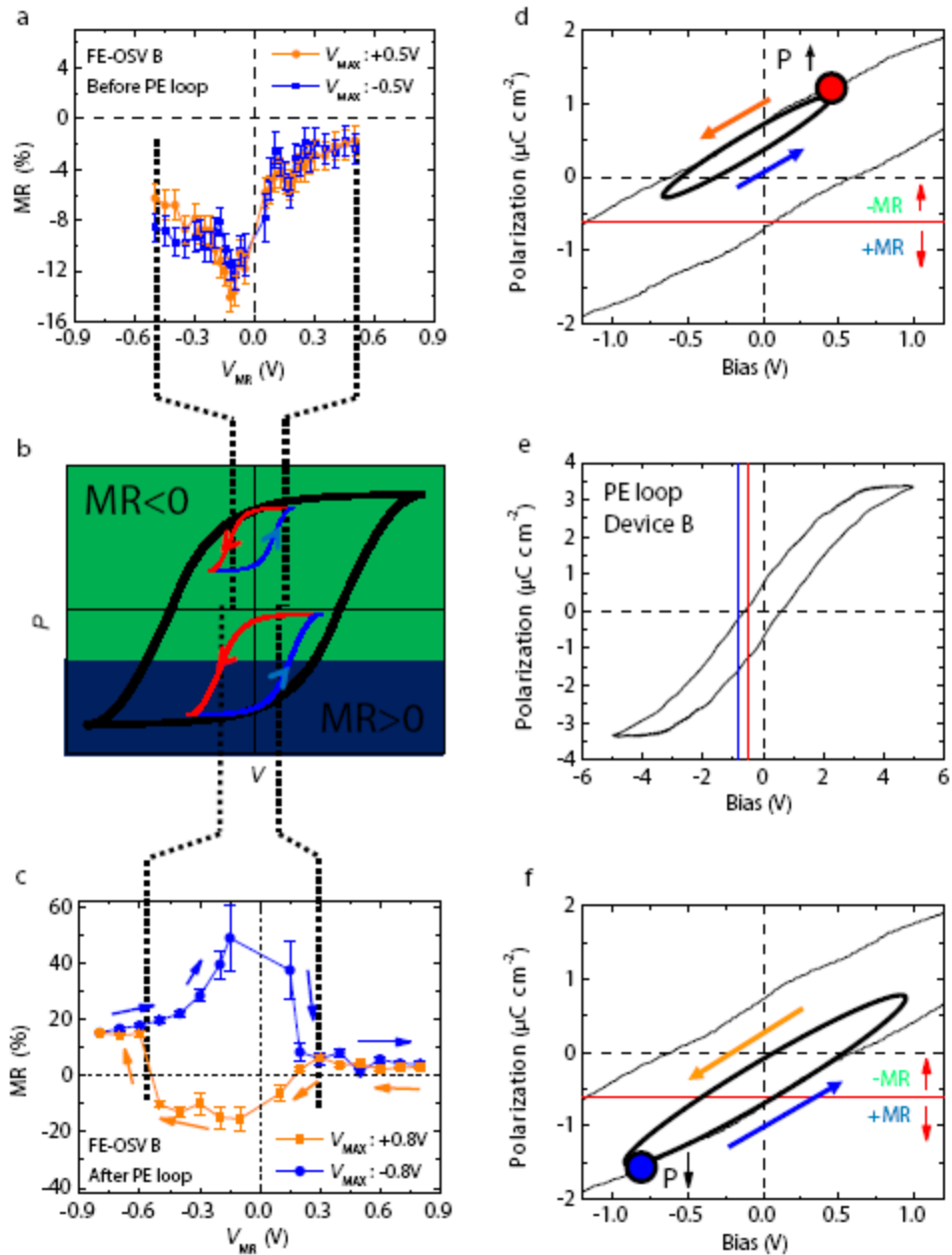
Supplementary Figure 8 | FE-MTJ control device a, MR loops of FE-MTJ at the same bias voltage (V_{MR} = -0.04V) but with two different V_{MAX} (+/- 2.0V). **b** to **d**, MR(V_{MR}) profiles as the dependence of V_{MAX}. No hysteretic behavior of MR is observed in the device. "**a1**" and "**a2**'" in **d** corresponds to the MR loops taken in **a** (V_{MAX}: +2.0V and -2.0V respectively). The measurements were taken at T=11K.

Supplementary Figure 9 | MR sign reversal. a and **c,** MR (V_{MR}) profile measured with as-grown PZT layer and PZT layer after polarization reversal respectively, as same as in **Fig. 4**. **b**, schematic correlation between the MR (V_{MR}) profile and the polarization of the PZT layer. **d to f**, The measured relation between polarization and voltage of the FE-OSV device. The yellow (blue) arrows indicated the direction of ramping the voltage V_{MAX} from positive to negative bias (negative to positive). Red (blue) spots present the starting polarization states of PZT.

SUPPLEMENTARY NOTES

Supplementary Note 1: Structural characterization using transmission electron microscopy (TEM)

The structure of the LSMO/PZT/Alq$_3$/Co (FE-OSV) devices was characterized by TEM. The deposited layers (Pt, Au, Co, Alq$_3$, PZT, and LSMO) can be distinguished by the contrast (see **Supplementary Fig. 1**) in the TEM image. The nominal thickness of the Co layer is 10 nm according to the calibration. The continuous layer of Co is 5 nm. The diffusion of Co atoms into Alq$_3$ is observed; but the low deposition temperature (280 K) suppresses the diffusion depth down to ~7 nm, which is much smaller than the measured thickness of Alq$_3$ layer (65 nm). The roughness of the interface between Alq$_3$ and Co is approximately 2 nm, which is also small. Therefore, the short circuit (possibly caused by the diffusion of Co atoms to the LSMO electrode) is unlikely in the FE-OSV devices in this work.

Supplementary Note 2: Measurement protocol of the MR (V_{MR}) profiles

The magneto-resistance (MR) is obtained by sweeping the magnetic field when the bias is fixed at a certain value (V_{MR}). In order to have a well-defined polarization state for the PZT during the MR measurements, the following protocol of bias voltage history is followed. Step (1): The bias voltage is slowly ramped to a high value V_{MAX} to restore the polarization of the PZT. Step (2): The bias voltage is slowly ramped to V_{MR}. Step (3): The MR loop is measured while the bias voltage is fixed at V_{MR}. Step (4): The bias voltage is slowly ramped to zero. **Supplementary Fig. 2a** shows an example of the bias voltage history for V_{MAX} = +1.2 V and V_{MR} = +0.5V. **Supplementary Fig. 2b** shows an example of the bias voltage dependence of the MR [or MR(V_{MR}) profile] where V_{MAX} is a constant value of +1.2 V. **Supplementary Fig. 2c** shows an example of the bias voltage history for V_{MAX} = -1.2 V and V_{MR} = -0.3 V. **Supplementary Fig. 2d** shows an example of MR (V_{MR}) profile where V_{MAX} is a constant value of -1.2 V. A clear hysteretic effect is observed by the difference between **Supplementary Fig. 2b** and **d**: the MR (V_{MR}) profile is strongly affected by the history of the bias voltage (Fig. 2e) which also determines the polarization state of the PZT.

Supplementary Note 3: Magnetometry measurement using a superconducting quantum interference device (SQUID)

In the OSV devices, two magnetic electrodes of intrinsically different magnetic coercive fields (LSMO and Co in this work) are chosen so that both parallel and antiparallel alignments of magnetizations of the electrodes can occur depending on the history of the applied magnetic field. The field dependences of the magnetizations of the FE-OSV devices are measured to verify the two different coercive fields. As shown in **Supplementary Fig. 3**, the two-step magnetization consists of a "soft" component and a "hard" component which presumably correspond to LSMO and Co respectively. The antiparallel alignment of the magnetization of the two electrodes can be obtained between the two steps. According to **Supplementary Fig. 3**, the coercive field of the

"soft" component is less than 100 Oe and the saturation field for the "hard" component is larger than 500 Oe.

As shown in **Supplementary Fig. 1**, the noticeable interdiffusion between the Co and Alq$_3$ layers is expected to affect the coercive field of Co electrodes due to the interfacial roughness, proximity effect or mixing between Co and Alq$_3$ molecules. The size distribution of the Co particles within the interdiffusion region may cause a distribution of the coercive field and saturation field. Under the same growth condition (thickness, deposition rate, deposited temperature for Alq$_3$ and Co), the coercive and saturation field of Co electrodes still vary for different devices, as shown in **Supplementary Fig. 3** for device A and B. These differences may cause the differences in the MR loops for two devices. Noted that the switching fields for LSMO electrodes are similar in both devices since LSMO is not affected by the interdiffusion.

Supplementary Note 4: Uncertainties of the MR measurements

The measurement uncertainties of the MR come from both statistical and systematic sources, i.e. statistical uncertainty and systematic uncertainty. In principle, the statistical error can be minimized by increasing the number of measurements. However, the long measurement time allows typically only 4 measurements. Therefore, the final measurement uncertainties include significant contributions from both statistical and systematic contributions. The operational estimation of the MR measurement uncertainties (error bars) are explained as the follows.

Statistical uncertainty

Supplementary Fig. 4 shows the MR measurements in a typical FE-OSV device at low temperature. The $R(H)$ relations of a single and multiple measurements (scans) are displayed in **Supplementary Fig. 4 a** and **b** respectively, where R is the resistance and H is the magnetic field. The background noise of the resistance measurements leads to a certain uncertainty of the MR measurements, which is defined as the statistical uncertainty of the MR measurements. It is clear that the background noise is reduced as the number of measurements is increased. The statistical uncertainty of the MR measurements is reduced accordingly, as shown in **Supplementary Fig. 4c**. Considering the tradeoff between the measurement time and measurement uncertainty, the MR values shown in the main text correspond typically to the result of 4 measurements.

Systematic uncertainty:

In addition to the statistical uncertainty, the systematic uncertainty in the MR measurement is also present. Since the systematic uncertainty comes from the imperfection of the measurement setup and the samples, they may or may not be easily estimated. One way of estimating the systematic error is by observing the asymmetry of the $R(H)$ relations. It is noticed that the $R(H)$ dependence is not totally symmetric about H=0. This asymmetry has been observed previously in organic and inorganic magnetoresistive devices. As shown in **Supplementary Fig. 4a** and **b**, the asymmetry persists even after averaging over many measurements. On the other hand, the trends of the MR calculated for the magnetic field ramping "up" and "down" (black) are similar, as shown in **Supplementary Fig. 4d**. In this work, we define MR as the average of the two values measured from the branch when the magnetic field is ramping "up" and from branch when the magnetic field is ramping "down". The differences between the two MR values are taken as the systematic uncertainty. Note that the comprehensive estimation of the systematic uncertainty is

very difficult. So the way we use here may still underestimate the systematic uncertainty.

Estimation of the total MR measurement uncertainty (error bar)

As discussed above, the total MR uncertainty are calculated considering both the statistical and systematic uncertainties:

$\sigma_{total} = \sigma_{sys} + \sigma_{stat}$, where σ_{sys} and σ_{stat} are the systematic and statistical uncertainty respectively. We define $\sigma_{sys} = \frac{|MR_L - MR_R|}{2}$.

For example, in **Supplementary Fig. 4d**, the total MR measurement uncertainty ($V_{MAX} = +0.5V$, $V_{MR} = -0.3V$) resulting from four $R(H)$ measurements is

$\sigma_{total} = \sigma_{sys} + \sigma_{stat} = \frac{|8.5\% - 7.2\%|}{2} + 0.6\% = 1.25\%$.

Here, the magnitudes of σ_{sys} and σ_{stat} are similar, and the error bars σ_{total} estimated using this method satisfy the Poissonian statistics, which is the case in most measurements. In rare case that σ_{total} is small, we manually enlarge the error bars (roughly 2 times) according to the dispersion of the data to satisfy the Poissonian statistics.

Reproducibility of MR loops

To further demonstrate the robustness of the hysteresis behavior of MR (V_{MR}) profiles, **Supplementary Fig. 5a** and **b** shows MR loops measured at -0.2V and -1.0V, respectively, after three ramping voltages ($V_{MAX}[I] = -1.2V$, $V_{MAX}[II] = +1.2V$ and $V_{MAX}[III] = -1.2V$). After a full cycle of ramping voltage, the resistance and the MR loops are nearly identical to that measured before the cycle (**Supplementary Fig. 5c**). The hysteretic effect coming from the sample drift could be excluded.

Supplementary Note 5: Control experiments for dependence of MR on V_{MAX}:

No dependence of MR on V_{MAX} in a LSMO-OSV control device

A conventional organic spin valve device without PZT (LSMO/Alq$_3$/Co, or LSMO-OSV) was grown as a control device (**Supplementary Fig. 6**). The MR (V_{MR}) profiles are similar for different V_{MAX}. In particular, the shift of the MR (V_{MR}) profile is negligible small. The dependence of the shift (ΔV) on V_{MAX} is shown in **Fig. 2f** of the main text.

No MR shift in STO-OSV device

We also fabricated an organic spin valve LSMO/STO/Alq$_3$/Co (STO-OSV) as a control device in which the 5 nm PZT layer is replaced with a 5 nm STO layer. Here the STO layer is a tunneling barrier but without dipole moment. Energy level diagrams of STO-OSV and FE-OSV are shown in **Supplementary Fig. 7a** and **b**, respectively. The $R(H)$ profiles are shown in **Supplementary Fig. 7c** and **d**. No significant shift of MR(V_{MR}) profile is observed for two different V_{MAX} (0.65V

and -0.65V) in **Supplementary Fig. 7e**. **Supplementary Fig. 7f** exhibits a surface of atomic flatness of STO (5nm) grown on LSMO/STO substrates, which is similar to that of PZT on LSMO/STO (**Fig. 1b**).

Significant dependence of MR on V_{MAX} but no shift in the MR(V_{MR}) profile in FE-MTJ device

In the main text, we show that for FE-OSV, the MR(V_{MR}) profiles depend strongly on V_{MAX}. More specifically, the MR(V_{MR}) profiles appear to be shifted by V_{MAX}. The shift is attributed to the change of effective voltage on the Alq$_3$ layer due to the vacuum level shift caused by the polarization of the PZT layer. To gain more insight on this mechanism, we fabricated ferroelectric magnetic tunnel junctions (LSMO/PZT/Co, or FE-MTJ) as the third control device. Co electrodes (area 200 μm*200 μm) are thermally deposited on top of PZT (5 nm)/LSMO (30 nm) substrates using a shadow mask, followed by an Au capping layer (10 nm).

Supplementary Fig. 8a shows two MR loops at the same bias voltage (V_{MR}: -0.04V) but with two V_{MAX} (+2.0V, -2.0V). **Supplementary Fig. 8b** to **d** show that MR(V_{MR}) profile with different V_{MAX}. Clear dependence of MR on V_{MAX} is observed, particularly in **Supplementary Fig. 8d**. However, the MR (V_{MR}) profiles show no significant shift for different V_{MAX}. These observations confirm the conclusion in Nat. Mater. 11, 289–293 (2012). In addition, it suggests that the change of MR by V_{MAX} in the FE-MTJ device is caused by a different mechanism. Note that in FE-MTJ, the PZT layer is sandwiched by two conductors (LSMO and Co). The dipole moment of the PZT layer is expected to be screened by the two electrodes, generating no vacuum level shift, which is consistent with the absence of the MR (V_{MR}) profile shift in the FE-MTJ device.

Supplementary Note 6: MR sign reversal by reversing the polarization of the PZT layer

As shown in **Supplementary Fig. 9a**, the MR (V_{MR}) of the FE-OSV device with the as-grown PZT layer show a small shift between V_{MAX} = +/-0.5V. The switchability of the polarization of the PZT layer is confirmed by hysteretic polarization-voltage loop, shown in **Supplementary Fig. 9e**. The polarization of the PZT layer is reversed by stopping the measurement of the hysteretic loop at -5 V. After the reversal of the polarization of the PZT layer, the MR (V_{MR}) profiles show dramatic change for different V_{MAX}. Even the sign of MR is changed from negative to positive in certain ranges of V_{MR} (**Supplementary Fig. 9c**). By comparing the MR (V_{MR}) profiles and the possible minor loops of the polarization-voltage relation during the measurement of the MR (V_{MR}) profiles (**Supplementary Fig. 9d to f**), a simple correlation between the sign of MR and electric polarization can be summarized (**Supplementary Fig. 9b**): MR is positive if the polarization of the PZT layer is below a certain (negative) value. Note that the threshold is not zero, suggesting that the mechanism of the sign reversal of the MR has to do with the detailed electronic structure of the electrodes. A proposed mechanism based on the electronic structure of LSMO is depicted in **Fig. 5** of the main text.